Numerical Investigation of Influential Factors in Hydraulic Fracturing Processes Using Coupled Discrete Element-Lattice Boltzmann Method

Weiwei Zhu[1], Zhiqiang Chen[2], Zhiguo Tian[1], Moran Wang[1]

[1]Department of Engineering Mechanics, Tsinghua University, Beijing, China
[2]Petroleum Exploration and Production Research Institute, SINOPEC, Beijing, China

Key Points:

- Different influential factors have significant impacts on the initiation pressure.
- High injection rates and heterogeneity degrees increase the geometrical complexity of fractures.
- Hydraulic fractures are dominated by tensile fractures, but shear fractures are also possible.

Abstract

Hydraulic fracturing is widely used to stimulate unconventional reservoirs, but a systematic and comprehensive investigation into the hydraulic fracturing process is rare. In this work, a discrete element-lattice Boltzmann method is implemented to simulate the hydro-mechanical behavior in a hydraulic fracturing process. Different influential factors, including injection rates, fluid viscosity, in-situ stress states, heterogeneity of rock strengths, and formation permeability, are considered and their impacts on the initiation and propagation of hydraulic fractures are evaluated. All factors have a significant impact on the fracture initiation pressure. A higher injection rate, higher viscosity, and larger in-situ stress increase the initiation pressure, while a higher formation permeability and higher heterogeneity decrease the initiation pressure. Injection rates and heterogeneity degrees have significant impacts on the complexity of generated fractures. Fluid viscosity, in-situ stress states, and formation permeability do not change the geometrical complexity significantly. Hydraulic fractures are usually tensile fractures, but many tensile fractures also have shear displacement. Shear

Corresponding author: Moran Wang, mrwang@tsinghua.edu.cn

fractures are possible and the shear displacement can be significant under certain conditions, such as a high injection rate, and a high heterogeneity degree.

Plain Language Summary

Hydraulic fracturing technique is essential for the development of unconventional reserves, such as shale gas, shale oil, and geothermal reservoirs. To optimize hydraulic fracturing operations and enhance recovery efficiency, it is necessary to understand the process's mechanism and figure out the influential factors. Direct observations of the hydraulic fracturing process in the subsurface are impossible. In this work, we adopt a numerical scheme (DEM-LBM) to investigate the process in detail and consider as many factors as possible, including injection rates, fluid viscosity, in-situ stress states, heterogeneity of rock strengths, and formation permeability. The impacts of those influential factors on the initiation and propagation of hydraulic fractures are evaluated. We find that all factors have a significant impact on fracture initiation pressure. However, the complexity of generated fractures is mainly affected by injection rates and heterogeneity degrees of rock strengths. Generated hydraulic fractures are usually tensile fractures, but shear fractures are possible and the shear displacement can be significant under certain conditions, such as a high injection rate, and a high heterogeneity degree. Continued research is required to further include the interactions between factors and it is completely possible with the foundation constructed in this work.

1 Introduction

Hydraulic fracturing refers to the process of injecting highly-pressurized liquid into a well to break up bedrock formations, which is vastly implemented in stimulating unconventional reservoirs, e.g. shale oil, shale gas, and enhanced geothermal systems (Pruess, 2006; Gandossi & Von Estorff, 2013).

The hydraulic fracture process is quite complex and cannot be observed directly in the deep subsurface. Microseismicity techniques are effective to locate fracture events and distinguish failure modes but cannot provide detailed information on fracture initiation and propagation (N. Warpinski et al., 2004; H. Chen et al., 2018). Therefore, many lab experiments and numerical simulations are conducted to investigate the hydraulic fracturing process. Experiments under triaxial and true triaxial stress conditions are widely adopted to mimic the actual geostress states (Huang & Liu, 2017; X. Zhao et al., 2019). The

acoustic emission method is used to monitor the hydraulic fracturing process (Stanchits et al., 2014; Goodfellow et al., 2015), but similar to the microseismicity method in the field, detailed morphology information of fractures is not available. To observe the fracture morphologies inside rock samples, Liu et al. (2018) experimentally investigated the hydraulic fracturing process in heterogeneous samples under different stress anisotropy levels and the morphological patterns of hydraulic fractures are identified with CT scanning. Similar methods are adopted by Yushi et al. (2016), Kumari et al. (2018), and many others. CT scanning method is limited to the resolution and long operation time, which is difficult to capture the real-time variations of fracture initiation and propagation process. In addition, hydraulic fracturing experiments are destructive experiments, which means the samples are not reusable after fracking. 3D-printed samples can reproduce the same rock samples and optical visualization is available (Liu et al., 2016), but the printing materials are usually far different from actual rocks in terms of physical and mechanical properties. Also, having a comprehensive investigation of the influential factors requires a large number of rock samples, which is both time-consuming and financially expensive.

Numerical simulation of the hydraulic fracturing process is a useful way to conduct sensitivity analysis of influential factors. The hydraulic fracturing process is a strongly coupled hydro-mechanical process. For the mechanical part, several continuum and mesoscale numerical methods are used to simulate fracture initiation and propagation. The continum methods mainly include the boundary element method (Olson & Taleghani, 2009; Cheng et al., 2022), extended finite element method (XFEM) (Dahi-Taleghani & Olson, 2011; Mohammadnejad & Khoei, 2013), and phase field methods (Wilson & Landis, 2016; Heider, 2021). However, the continuum method usually involves high requirements for mesh quality and complicated treatments for complex boundary conditions. Therefore, the mesoscale numerical method is also widely used to simulate mechanical deformation, which mainly refers to the discrete element method (DEM). DEM directly describes the mechanical displacements and interactions of discontinues particles (Cundall & Strack, 1979). For the fluid dynamics part, the assumption of lubrication flow is usually used since a fracture has a width significantly smaller than its length. The finite volume method (FVM) and finite element method (FEM) can be used to discretize and solve the flow equations and couple with mechanical part (Peirce & Detournay, 2009; Lecampion, 2009; Wangen, 2011; Papachristos et al., 2017). However, the lattice Boltzmann method (LBM) has several advantages compared with FVM and FEM, such as simple calculation procedures, convenient

implementation of parallel computation, and simple treatment of complex geometries. In addition, through the Chapman-Enskog theory, the Navier-Stokes equations can be derived from the Boltzmann equation (S. Chen & Doolen, 1998). Therefore, the LBM method can solve the Navier-Stokes equations and overcome the possible inaccuracy caused by the lubrication flow assumption. Coupled DEM-LBM method is a good option for simulating the hydro-mechanical coupling process (S. A. Galindo-Torres et al., 2012; S. Galindo-Torres, 2013; Z. Chen & Wang, 2017; Z. Chen et al., 2020).

Many factors can influence the geometry of hydraulic fractures, like formation parameters (e.g. in-situ stress), treatment parameters (e.g. injection rate and fluid viscosity), and rock properties (e.g. rock strength heterogeneity and formation permeability). Zeng and Roegiers (2002); De Pater and Beugelsdijk (2005); Liu et al. (2018); Zhuang et al. (2019); Fazio et al. (2021) and Y. Zhao et al. (2022) investigated the impact of injection rate, fluid viscosity, stress states, and matrix permeability on the hydraulic fracturing process with lab experiments. The results provide helpful insights, but lab experiments cannot use an identical rock sample in each test. A strict factor control leads to a large number of individual experiments and lab experiments usually cannot exclude the impact of intrinsic rock characteristics, such as the heterogeneity of natural rocks. In contrast, numerical simulations can have better factor controls and investigate the impact of each factor. Nagaso et al. (2015); Wang et al. (2016); Z. Chen et al. (2020) and Duan et al. (2018) investigated the impact of fluid viscosity, injection rate, and in-situ states on the fracture propagation process through different numerical methods. However, a comprehensive investigation of the hydraulic fracturing process considering all the influential factors mentioned above is rare (Zhuang & Zang, 2021). In this work, we aim to have a comprehensive investigation considering the impacts of injection rate, fluid viscosity, heterogeneity of rock strength, formation permeability, and in-situ stress state on the initiation and propagation of hydraulic fractures, which is helpful to deepen the understanding of hydraulic fracturing processes.

In this work, a DEM-LBM method is adopted to simulate the hydraulic fracturing process, and Section. 2 introduces detailed information about the coupled method. Impacts of different factors on fracture initiation and propagation are demonstrated in Section. 3. In Section. 4, we discuss the limitation of the method and possible improvements. Important conclusions are summarized in Section. 5.

2 Methods and materials

2.1 A DEM-LBM scheme for the simulation of hydraulic fracturing process

A DEM-LBM method is adopted in this work to simulate the coupled hydro-mechanical process. The numerical framework is based on the multi-physics simulation software MECHSYS developed by S. Galindo-Torres (2013) and extension of the software developed by Z. Chen and Wang (2017) and Z. Chen et al. (2018, 2020). Only a brief introduction of the method is covered in this section and more detailed information is available in the references above.

DEM treats materials as an assembly of discrete particles. In this work, the interactions between particles are approximated with linear contact and bonding models. In the linear contact model, the contact can happen between different geometrical patterns of two particles, including edge-edge and vertex-face for polyhedrons (S. A. Galindo-Torres et al., 2012). The normal elastic force $\vec{F_n^c}$ between different geometrical pairs (P_i and P_j) is given by:

$$\vec{F_n^c}(P_i, P_j) = K_n \vec{\delta}(P_i, P_j), \tag{1}$$

Where K_n is the normal contact stiffness, $\vec{\delta}(P_i, P_j)$ is the normal displacement (overlapping) vector between a geometric pattern pair. The net elastic force is the summation of forces for all pairs of geometrical patterns.

Similarly, the tangential contact force $\vec{F_t^c}$ is given by:

$$\vec{F_t^c} = K_t \vec{\zeta}(P_i, P_j), \tag{2}$$

where K_t is the tangential contact stiffness and $\vec{\zeta}(P_i, P_j)$ is the tangential displacement vector between a geometric pattern pair.

In the bonding model, two neighboring spheropolyhedra sharing a common face are connected with an elastic force. The cohesive force in the normal direction $\vec{F_n^b}$ is given by:

$$\vec{F_n^b} = B_n A \vec{\epsilon}_n, \tag{3}$$

where B_n is the normal elastic modulus of the material, A is the shared face area between particles, and $\vec{\epsilon}_n$ is the normal strain in the direction normal to the common face and positive for tensile deformation. The normal cohesive force is calculated for tensile deformation only and Eq. 1 accounts for the normal elastic force in a compressive deformation.

The cohesive force in the tangential direction $\vec{F}_t^b$ is given by:

$$\vec{F}_t^b = B_t A \vec{\epsilon}_t, \tag{4}$$

where B_t is the tangential elastic modulus of the material, and $\vec{\epsilon}_t$ is the shear strain in the direction tangential to the common face.

A threshold value on the total strain, denoted as ϵ_{th}, is provided as the criterion of fracture initiation:

$$|\vec{\epsilon}_n| + |\vec{\epsilon}_t| \geq \epsilon_{th}, \tag{5}$$

where $\vec{\epsilon}_n$ and $\vec{\epsilon}_t$ are the normal and tangential strain caused by the displacement of adjacent faces.

A broken bond is classified as a shear failure if its shear strain is larger than the normal strain. Similarly, a tensile failure refers to a case where the tensile strain is larger than the shear strain. A similar classification is adopted in Shimizu et al. (2011) and Z. Chen and Wang (2017).

The lattice Boltzmann method (LBM) is a useful computational fluid dynamics method for fluid simulation, where the fluid is regarded as fictive particles, and the density distribution functions of particles are simulated through streaming and collision processes. In this work, a D3Q15 model is chosen to simulate the fluid flow considering the accuracy and computation efficiency. The corresponding evolution equation is:

$$f_i(\vec{x} + \vec{e_i}\delta t, t + \delta t) = f_i(\vec{x}, t) - \frac{\delta t}{\tau}(f_i(\vec{x}, t) - f_i^{eq}(\vec{x}, t)), \qquad i = 0, 1, 2...14, \tag{6}$$

where f_i and f_i^{eq} are the density distribution function and the corresponding equilibrium distribution in the ith discrete velocity direction, $\vec{e_i}$, δt is the time step adopted in the simulation, and τ is the relaxation time. Through the Chapman-Enskog analysis, the fluid kinematic shear viscosity ν is related to τ by:

$$\nu = \frac{1}{3}c^2(\tau - \frac{\delta t}{2}), \tag{7}$$

where c is the lattice speed in LBM. Note that all parameters in lattice Boltzmann equations are dimensionless with "lattice units". To map the lattice units to physical units, proper conversion factors are required. A set of basic conversion factors, composed of time, length, and mass, is sufficient to derive the dimension of any physical parameters in this work. The corresponding basic conversion factors are C_l, C_t, and C_ρ, since the length, time and density

are natural quantities in LB simulations.

$$C_l = \frac{\delta x^*}{\delta x} \tag{8}$$

$$C_t = \frac{\delta t^*}{\delta t} \tag{9}$$

$$C_\rho = \frac{\rho^*}{\rho} \tag{10}$$

Note that the parameters with * have physical units. δx and δt are the grid size and time step used in the simulation. Usually, δx and δt are 1 in LBM implementation and we use the physical density as the lattice density. Therefore, the corresponding conversion factors are $C_l = \delta x^*$, $C_t = \delta t^*$, and $C_\rho = 1$. The conversion factor for ν can be obtained through a simple dimension analysis:

$$C_\nu = \frac{C_l^2}{C_t} \tag{11}$$

Therefore, the physical kinematic viscosity of the simulated fluid is

$$\nu^* = \frac{1}{3}(\tau - \frac{1}{2})\frac{\delta^2 x^*}{\delta t^*} \tag{12}$$

The fluid density and velocity can be obtained from the density distribution function:

$$\rho = \sum_i f_i \tag{13}$$

$$\vec{u} = \frac{\sum_i f_i \vec{e_i}}{\rho} \tag{14}$$

The pressure can also be obtained from the Chapman-Enskog analysis:

$$p = \frac{1}{3}\rho c^2 \tag{15}$$

In the fluid simulation, we care more about the pressure difference concerning the initial pressure instead of the specific pressure. Therefore, with a proper conversion factor, the physical pressure difference can be calculated by:

$$\Delta p^* = \frac{1}{3}\Delta\rho\frac{\delta^2 x^*}{\delta^2 t^*} \tag{16}$$

An immersed boundary method (IBM) is applied to incorporate the fluid-solid interactions (Noble & Torczynski, 1998; Z. Chen & Wang, 2017). The basic logic behind the IBM method is that the fluid flow is simulated in the whole domain including the particles. For fluid inside a particle, a body force is inserted to make the fluid have the same rigid movement as the particle and the no-slip boundary condition is fulfilled for the external fluid flow. A fluid-solid interaction term Ω_i^{fs} is added in the standard LBM evolution equation.

$$f_i(\vec{x} + \vec{e_i}\delta_t, t + \delta t) = f_i(\vec{x}, t) + (1 - B)\{-\frac{\delta t}{\tau}(f_i - f_i^{eq})\} + B\Omega_i^{fs}, \tag{17}$$

where B is a weighting parameter, which is a function of τ and the solid volume fraction γ:

$$B = \frac{\gamma(\tau/\delta t - 1/2)}{(1-\gamma) + (\tau/\delta t - 1/2)}, \tag{18}$$

where γ is defined as the ratio of the solid volume over the lattice volume. When $\gamma = 0$, there are no solids in the corresponding fluid lattice. When $\gamma = 1$, the lattice is fully occupied by the solid phase. When $B = 0$, corresponding to $\gamma = 0$ (fluid lattice), the evolution equation degenerates to the standard one. Ω_i^{fs} can be obtained from a "bounce-back" of the nonequilibrium part of the density distribution:

$$\Omega_i^{fs} = f_{-i}(\vec{x}, t) - f_i(\vec{x}, t) + f_i^{eq}(\rho, \vec{u}_s) - f_{-i}^{eq}(\rho, \vec{u}_s), \tag{19}$$

where f_{-i} refers to the "bounce-back" state from f_i by reversing all unit velocity vector, i.e. $\vec{e_i}$ to $-\vec{e_i}$, and u_s is the velocity of the solid particle at time $t + \delta t$ at the position $\vec{x}$. To obtain the solid velocity, a force analysis of the particle is required. However, in this work, the particles are assumed to be unmovable to avoid the numerical error caused by particle vibrations. For cases with non-negligible particle velocities, Z. Chen and Wang (2020) proposed an improved IBM method, which incorporates the inertial force term with a finite-difference expression.

In Appendix A and Appendix B, a gravity-driven Poiseuille flow in a slit and a Brazilian test are used to validate the correctness of LBM and DEM schemes.

2.2 Simulation setup

The simulation model considered is a rectangular plate with a width of 4.0 cm, length of 6.0 cm, and thickness of 1.28 mm. The solid particles are shown in red in Fig. 1(a) with a total number of 741. The solid particles are eroded and dilated to form channels for the fluid flow (shown in blue in Fig. 1). The solid volume fraction γ is used to control the initial permeability of the flow domain in the LBM lattice. For the whole flow domain, there is a predefined γ controlling the initial permeability of the matrix, which can be used to mimic the leakage of injected fluid to formation in reality. A small cave on the left side is assigned as the fluid inlet and the initial γ value is zero. A preset fracture is denoted in Fig. 1(a), which mimics the perforation process in reality and helps to intrigue the hydraulic fracture. The detailed simulation parameters are listed in Table. 1.

Four rectangular plates on each side of the domain are added to implement different stresses on the horizontal (left-right) and vertical (top-bottom) directions, shown in

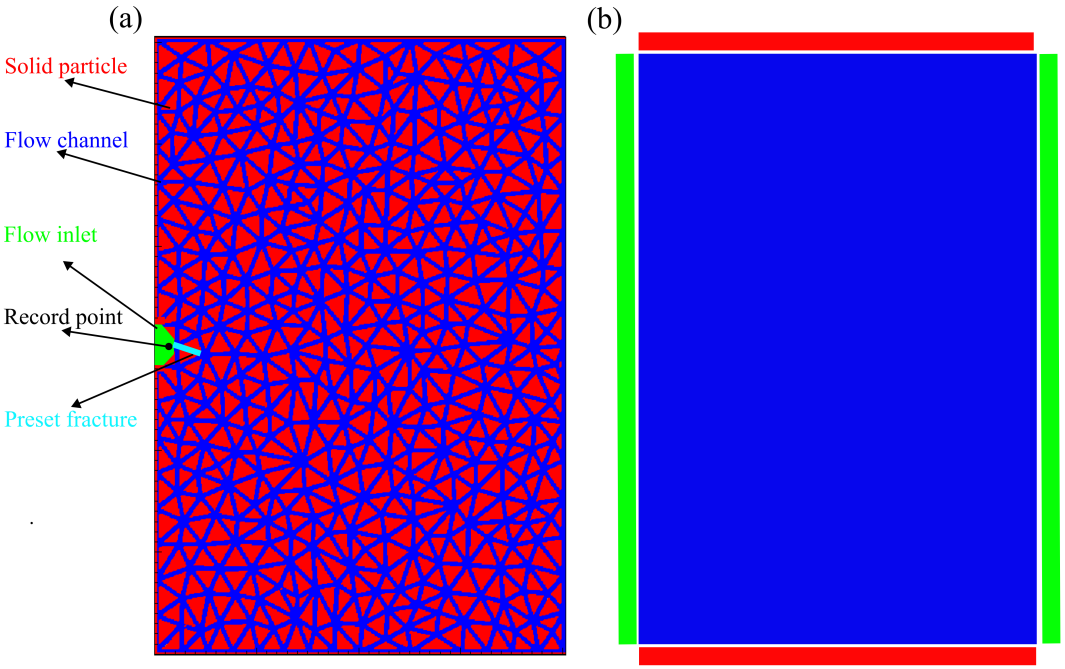

Figure 1. Calculation domain with a length of 6 cm, a width of 4 cm, and a thickness of 1.28 mm

Fig. 1(b). The horizontal and vertical plates have a length of 4.0×10^{-2} m and 6.0×10^{-2} m. The width and height of plates are the same as the thickness of the particle, 1.28×10^{-3} m. There is a constant flow-rate condition for the inlet and a fixed pressure is assigned on the right side of the domain. All the other boundaries are set as solid.

Since the discrete element method is only conditionally stable, the time step should be small enough to reach the convergence. The critical time step is a function of the particle mass, its stiffness, and its arrangement (O'Sullivan & Bray, 2004). To ensure the convergence, the time step fulfills the criterion below (S. A. Galindo-Torres et al., 2012):

$$\Delta t_{critical} = 0.1\sqrt{\frac{M_{min}}{C_{nmax} + B_{nmax}}}, \tag{20}$$

where M_{min} is the minimum mass of all particles, C_{nmax} and B_{nmax} are the maximum normal contact and bond stiffness of all particles, respectively. From Eq. 20, a larger value of the particle stiffness, a smaller time step is required. In this work, the heterogeneity of rock strengths is considered, which focuses more on the variations of rock strengths. Specific rock strengths are excluded as the influential factor. Therefore, we reduce the stiffness and modulus values to increase the time step as shown in Table. 1, which makes the simulation computationally affordable (Yousefi & Ng, 2017).

Table 1. Input parameters for the DEM-LBM simulation

Parameter	Value
Normal contact stiffness, K_n	1.0×10^6 N/m
Tangential contact stiffness, K_t	1.0×10^6 N/m
Normal elastic modulus, B_n	2.0×10^6 [Pa]
Tangential elastic modulus, B_t	4.2×10^6 [Pa]
Bond strength, ϵ_{th}	0.01 [-]
Fluid density, ρ_{f}^*	1.0×10^3 [kg/m^3]
Lattice size in LBM, δ_x^*	1.0×10^{-4} [m]
Time step in DEM/LBM, δ_t^*	1.0×10^{-6} [s]

If the bond strengths of all particles are the same, it will lead to a homogeneous rock sample. However, real rock samples are always heterogeneous because of different mineral compositions and cement materials. Therefore, the heterogeneous bond strengths are more appropriate for real rocks and it is one of the influential factors investigated in this work. The Weibull distribution is widely adopted to describe heterogeneous bond strengths for brittle rocks (Van Mier et al., 2002; Z. Chen & Wang, 2017; Pan et al., 2018; Z. Chen et al., 2020):

$$f(\epsilon_{th}) = \frac{m}{\epsilon_{th}^0}(\frac{\epsilon_{th}}{\epsilon_{th}^0})^{m-1} \exp(-(\frac{\epsilon_{th}}{\epsilon_{th}^0})^m), \tag{21}$$

where ϵ_{th}^0 is the average bond strength threshold and is set as 0.01 in this work. m is the shape parameter, describing the heterogeneity degree of the bond strength. An infinitely large m corresponds to a homogeneous structure, while a low value of m indicates a heterogeneous structure.

The influential parameters investigated in this work also include the injection rate and in-situ stress states. To properly choose the injection rate and the stress levels, we conducted a Buckingham analysis (Buckingham, 1915) with the following steps and scaled our simulation parameters with parameters in actual experiments.

- Choose possible variables: tensile strength S, viscosity of fluid ν, particle size l, injection rate q, fluid density ρ. In total, the number of variables is 5;
- Find variables with repeating units: particle size l, injection rate q, fluid density ρ. Therefore, the number of dimensions is 3 and the basis of fundamental units are

T (time), L (distance), and M (mass). Therefore, there should be two independent dimensionless parameters (π_1 and π_2) concerning fluid viscosity ν and tensile strength S.

- The first dimensionless parameter π_1:

$$\pi_1 = \nu \times l^a \times q^b \times \rho^c \tag{22}$$

The unit of π_1 is:

$$[\pi_1] = [\frac{L^2}{T}] \times [L]^a \times [\frac{L^3}{T}]^b \times [\frac{M}{L^3}]^c \tag{23}$$

Since π_1 is dimensionless, we have:

$$\pi_1 = \frac{\nu \cdot l}{q}, \tag{24}$$

which is similar to the Reynolds number, if l is the characteristic length of the flow channel.

- The second dimensionless parameter π_2:

$$\pi_2 = S \times l^a \times q^b \times \rho^c \tag{25}$$

The unit of π_2 is:

$$[\pi_1] = [\frac{M}{T^2 L}] \times [L]^a \times [\frac{L^3}{T}]^b \times [\frac{M}{L^3}]^c \tag{26}$$

Since π_2 is dimensionless, we have:

$$\pi_2 = \frac{S l^4}{q^2 \rho} = \frac{S}{\rho q^2 / l^4}, \tag{27}$$

where the denominator part is equivalent to the dynamic pressure term $\frac{1}{2}\rho u^2$.

To estimate proper injection rates and stress levels, we take the experiment parameters from Liu et al. (2018), i.e. $\mathrm{q} = 3.26 \times 10^{-7}$ m^3/s, $\nu = 6.7 \times 10^{-5} \mathrm{m}^2/\mathrm{s}$, $\mathrm{S} = 5.7 \times 10^6$ Pa, and $\rho = 1000$ $\mathrm{kg/m}^3$. The particle size l is estimated as 5.0×10^{-3}m for the glutenite rock used in the experiment. On the simulation side, we choose the dynamic viscosity as $\nu_\mathrm{s} = 5.0 \times 10^{-4}$ m^2/s and fluid density as $\rho_\mathrm{s} = 1000$ $\mathrm{kg/m}^3$. The particle size is estimated by $\mathrm{l_s} = 0.25\sqrt{\mathrm{A_{max}}}$, where $\mathrm{A_{max}} = 5.0 \times 10^{-6}$ m^2 is the maximum particle area in the simulation. Correspondingly, the injection rate in the simulation is estimated from π_1, $q_s = 2.72 \times 10^{-7}$ m^3/s, and the corresponding injection velocity is $u_s = 0.34$ m/s. From π_2, the proper magnitude of tensile strength can be estimated. Please note that the tensile strength in the simulation should be scaled according to the elastic modulus and failure criterion. As a result, a stress magnitude of 10 MPa in the experiment corresponds to

1.68×10^4 Pa in the simulation. In this way, proper values of injection rates and stress levels are found for the simulation with an appropriate magnitude.

3 Results

We systematically investigate the individual impact of injection rates, fluid viscosity, in-situ stresses, heterogeneous bond strengths, and formation permeability on fracture initiation and propagation. Each influential factor is evaluated with the other factors fixed at a reference value. The reference value for each parameter is listed as follows: 0.2 m/s for the injection velocity, 5.0×10^{-4} m^2/s for the fluid kinematic viscosity, no stress state for the in-situ stress states, homogeneous bond strengths for heterogeneous bond strengths and a solid volume fraction of 0.97 for the formation permeability.

3.1 Impact of injection rate

Six different injection velocities are chosen for the investigation under an unconfined condition: 0.1 m/s, 0.2 m/s, 0.3 m/s, 0.5 m/s, 0.8 m/s and 1.0 m/s. The pore pressure variations of the inlet position (the record point shown in Fig. 1a) are shown in Fig. 2. With injection velocity increases, the fracture initiation pressure also increases, consistent with many observations from lab experiments and numerical simulation (Morgan et al., 2017; Zhuang et al., 2019; Duan et al., 2018). For low injection velocities (u = 0.1 and 0.2 m/s), the pore pressure vibrates, but decreases with fracture propagation, which indicates that the fracture volume and leak-off volume expand at a roughly equal or a slightly greater rate than the injection rate. For high injection velocities (u > 0.2 m/s), the pore pressure continues to increase after the fracture initiation, indicating that the fracture volume and leak-off volume increase at a smaller rate than the injection rate.

The fracture geometries of each case are shown in Fig. 3 with the fluid pressure distribution shown in the background. The center point of each fracture is represented by a solid square for a tensile fracture and a circle for a shear fracture. The color variations from cold (blue) to warm (red) refer to the sequence of generation. For low injection velocity, the fracture geometries are almost the same (Fig. 3(a,b)). However, with the increasing injection velocities, the fracture geometries become complex with branches. The main horizontal fractures in different cases are similar. However, when the horizontal fracture reaches the right boundary, vertical fractures tend to form at a high injection velocity and most

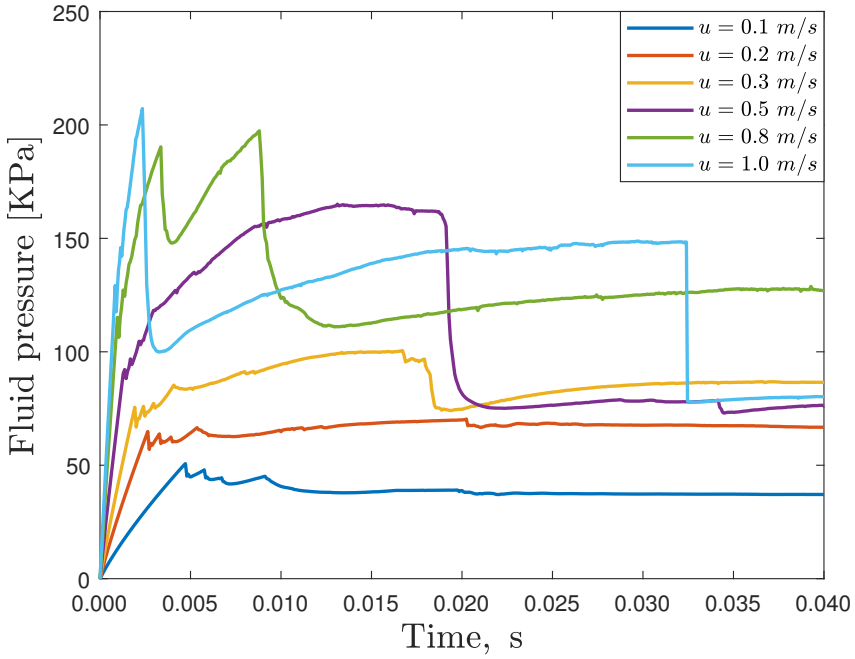

293 **Figure 2.** The pore pressure evolution at the record point for cases with different injection rates

317 fractures generated in the transition zones (from horizontal to vertical) are shear instead
318 of tensile fractures. When the horizontal fracture reaches the right boundary, the pore
319 pressure in the hydraulic fracture compresses the sample in the top-bottom direction. The
320 stress condition makes the newly generated fracture perpendicular to the horizontal fracture
321 because the fracture trace should be perpendicular to the minimum principle stress (zero
322 stress in the left-right direction). In addition, when the injection velocity is high, the pore
323 pressure becomes significantly high as shown in Fig. 2, which is large enough to generate a
324 new fracture in the top-bottom direction.

326 Fig. 4 shows the tensile and shear strain component of each fracture segment in Fig. 3.
327 The tensile and shear strains are represented with red and green circles, respectively. The
328 links between tensile and shear strain for tensile and shear fractures are light blue and
329 regular blue. When the injection rate is small, all fractures are tensile fractures with in-
330 significant shear strain between particles. However, when the injection rate increases, more
331 fractures have a comparable even larger shear strain than tensile strain. The proportion of
332 shear fractures increases with the increasing injection velocity, which is consistent with the
333 observation in Duan et al. (2018).

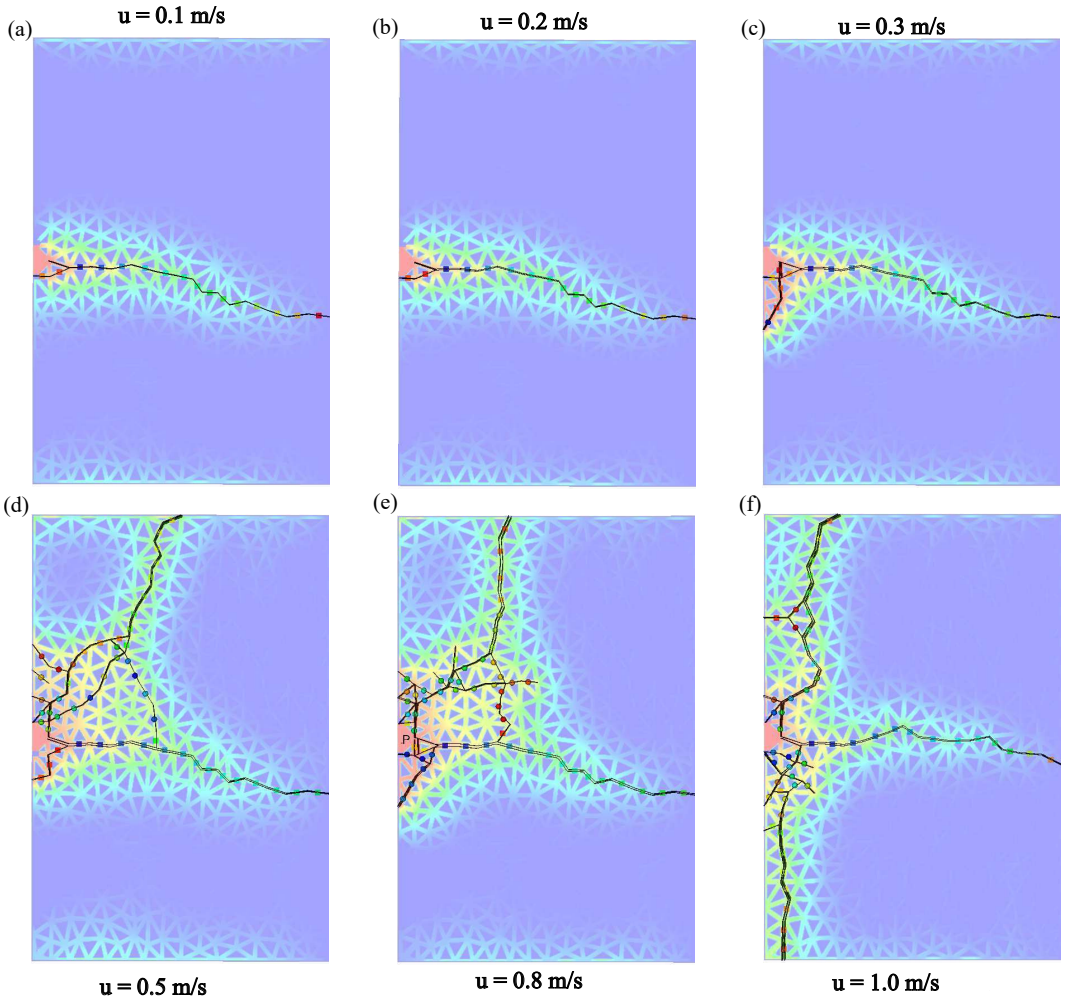

Figure 3. Fracture geometries of cases with different injection rates at 0.04s. The background shows the fluid pressure distribution in the entire domain. The center of each fracture segment is marked with squares for tensile fractures and circles for shear fractures. The color variations from blue to red refer to the generation sequence of each type of fractures.

3.2 Impact of fluid viscosity

Six levels of viscosity are chosen for the investigation under an unconfined condition: $\nu = 5.0 \times 10^{-5}$ m^2/s, 9.0×10^{-5} m^2/s, 2.0×10^{-4} m^2/s, 5.0×10^{-4} m^2/s, 1.0×10^{-3} m^2/s, 2.0×10^{-3} m^2/s. The pore pressure variations at the record point are shown in Fig 5. With viscosity increases, the initial stage of the pressure build-up of all cases is similar, but the initiation pressure increases for the case with a high viscosity. Similar results are observed in Duan et al. (2018) and Z. Chen et al. (2020). The fracture geometries are similar for different fluid viscosity and three examples are presented in Fig. 6. When the viscosity is

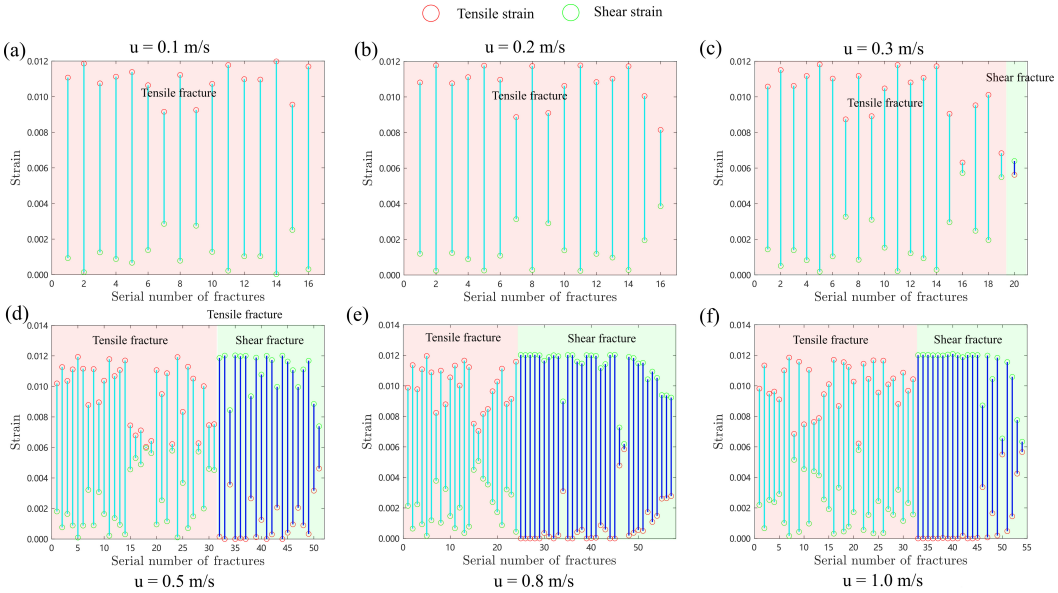

Figure 4. Tensile and shear strain of each fracture segment in Fig. 3

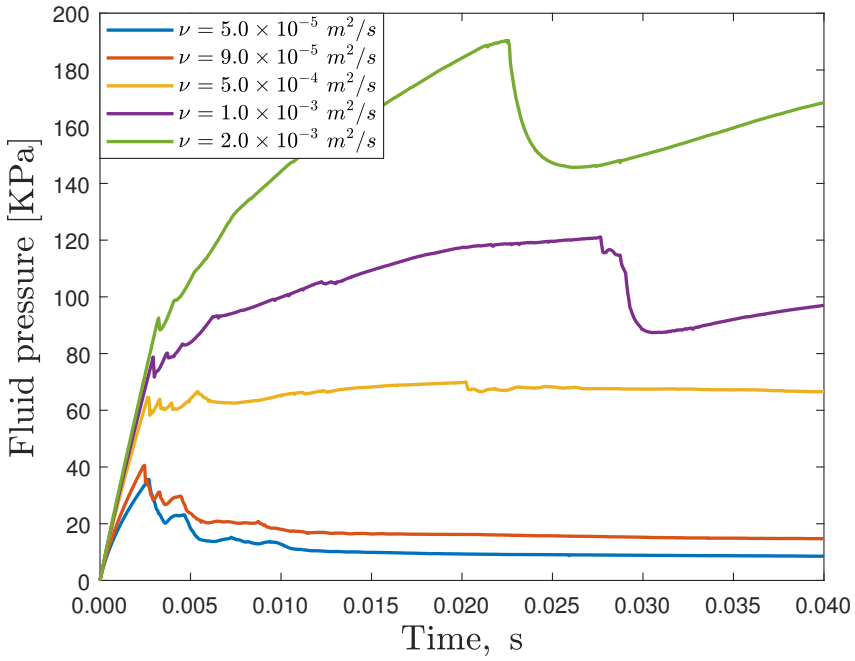

Figure 5. The pore pressure evolution at the record point for cases with different fluid viscosity

low, the fluid can leak into the formation easily and make the pore pressure of the formation increase as shown in Fig.6(a). Also, a few branches along the main hydraulic fracture can be observed in Fig. 6(a). For high-viscosity fluid, the pore pressure can only propagate to the neighboring region and the region area shrinks with increasing viscosity. In addition, after the horizontal fracture reaches the right boundary, new fractures can be generated at the

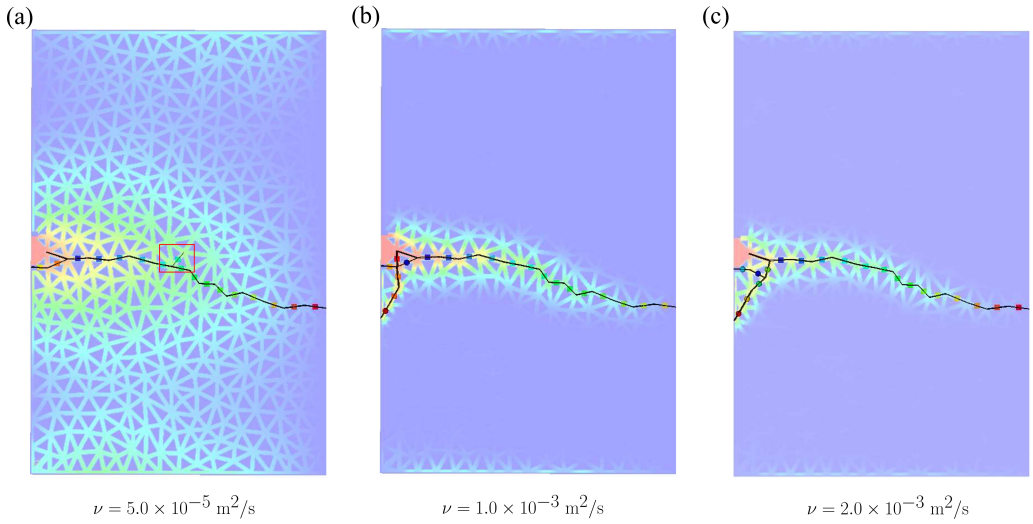

Figure 6. Fracture geometries of cases with different fluid viscosity at 0.04s. A branch generated in the low-viscosity case is marked in the red box.

inlet because of the high pore pressure therein as shown in Fig. 5. For the highest viscosity considered in this work, $\nu = 2.0 \times 10^{-3}$ m^2/s, the pore pressure continues to increase after 0.04 s as shown in Fig. 7(a). New fractures are generated in the vertical direction and continue to propagate as shown in Fig. 7(b). Most inclined fractures are shear fractures and the fractures become tensile in a perpendicular direction.

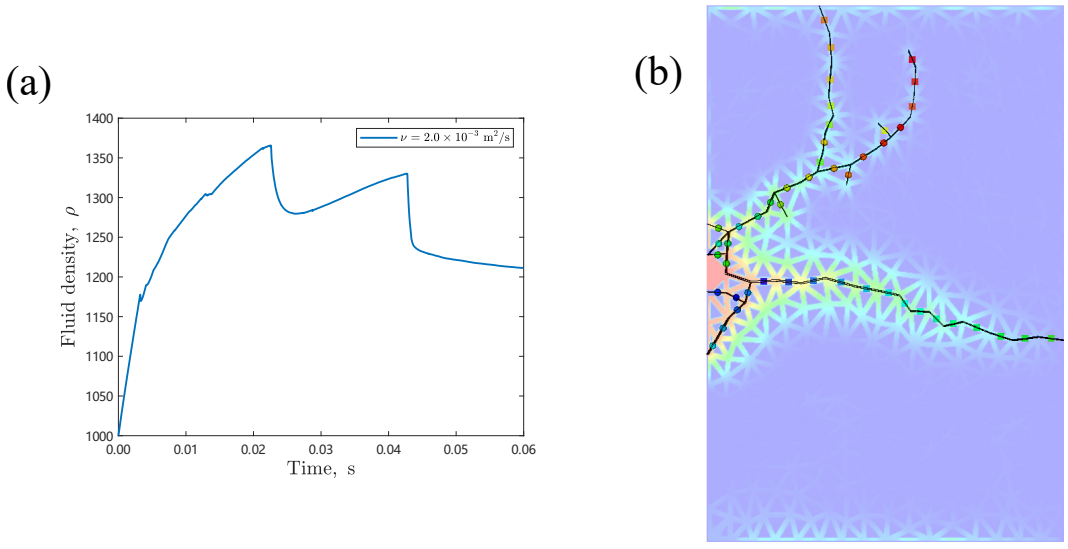

Figure 7. The pore pressure evolution at the record point for cases with high fluid viscosity, $\nu = 2.0 \times 10^{-3}$ m^2/s (a) and the corresponding fracture geometries (b) at 0.06s.

Fig. 8 presents the strain component of each fracture segment in Fig. 6. When the viscosity is low, all generated fractures are tensile fractures. With the increasing viscosity, the shear strain becomes more significant and the proportion of shear fractures also increases. However, the main horizontal fractures are mostly tensile and shear fractures are usually the newly generated inclined fractures.

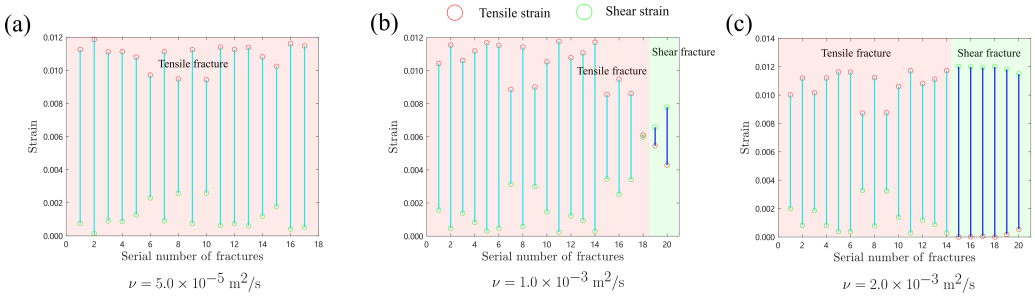

Figure 8. Tensile and shear strain of each fracture segment in Fig. 6

Fluid with low viscosity has stronger penetration capability than highly viscous fluid. Fig. 9 shows the pressure distribution of cases with low and high fluid viscosity at the fracture initiation stage. The pressure propagates much farther in the low-viscosity case. Similar observations are obtained from Duan et al. (2018) and Z. Chen et al. (2020). The penetration capability may not change the fracture geometries significantly in the homogeneous media since all bonds are equally strong. However, for heterogeneous media or formations with preexisting natural fractures, such penetration capability can help to generate more complex fracture geometries (Z. Chen et al., 2020).

3.3 Impact of in-situ stress states

The stress on the top-bottom direction is fixed at 1.68×10^4 Pa as derived in Section. 2. Different stress anisotropy degrees are represented by the stress ratio between σ_{lr} (left-right direction) and σ_{tb} (top-bottom direction). Six levels of the ratio are chosen for the investigation: $\sigma_{lr}/\sigma_{tb} = 1.0, 1.3, 1.5, 1.7, 1.9, 0$.

The pore pressure variations of each case at the record point are shown in Fig. 10, where the initiation pressure increases due to the imposed in-situ stresses. A larger imposed in-situ stress leads to a higher fracture initiation pressure. However, the implementation of

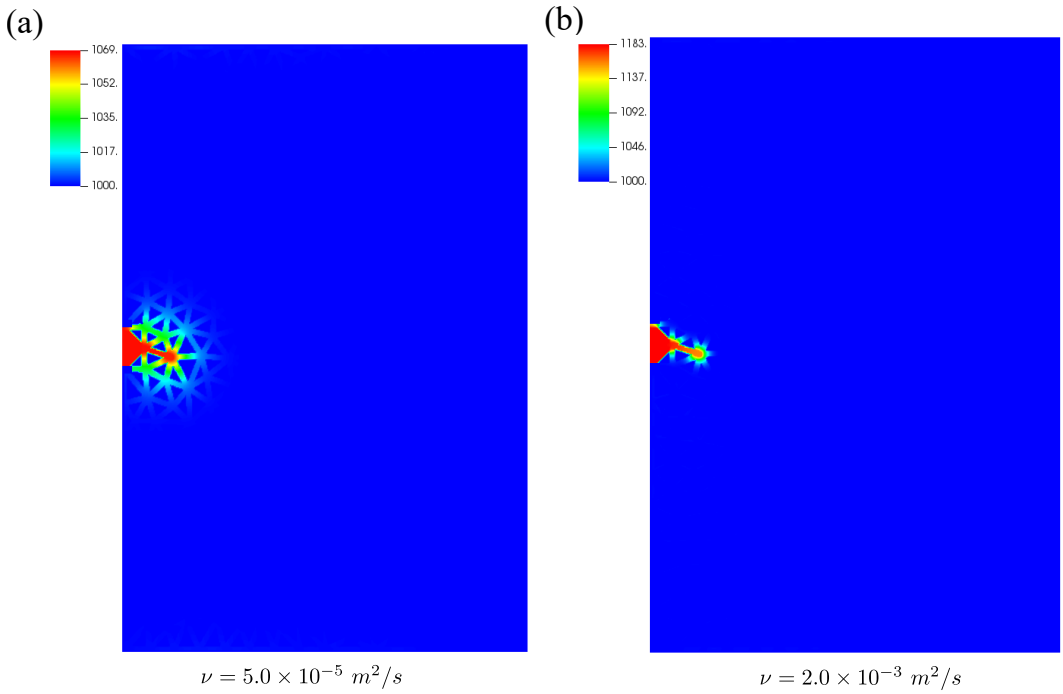

Figure 9. Pore pressure distribution at the fracture initiation stage for cases with a low(a) and high (b) fluid viscosity, respectively

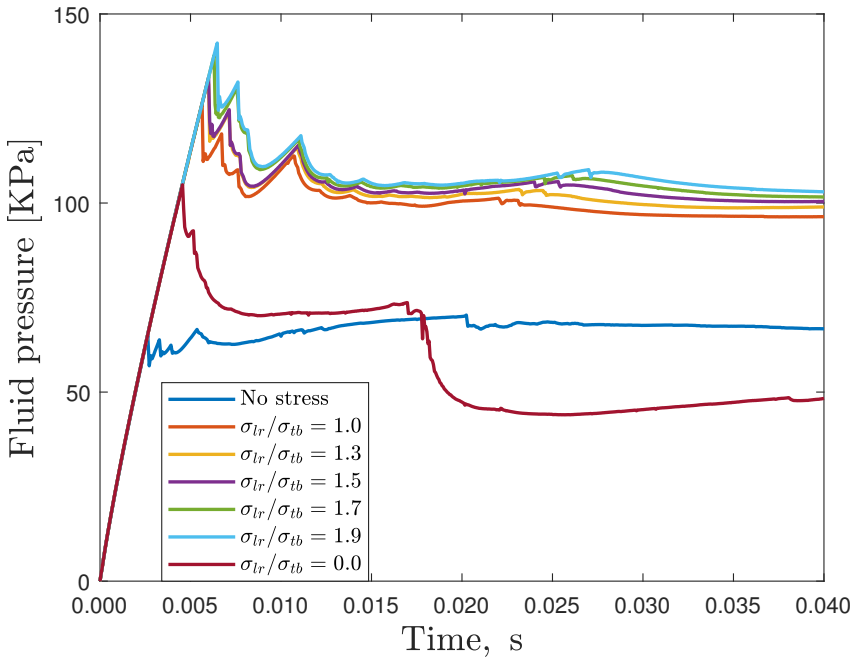

Figure 10. The pore pressure evolution at the record point for cases with different in-situ stress states

in-situ stress does not change the fracture geometry significantly. For the first five cases, where σ_{lr} is the maximum principle stress, the fracture geometries are similar and have a direction perpendicular to the minimum stress direction (top-bottom direction). Two examples of with $\sigma_{\mathrm{lr}}/\sigma_{\mathrm{tb}} = 1.0$ and 1.9 as shown in Fig. 11(a and b). For the case where no stress applies in the left-right direction, the fracture propagates in the top-bottom direction as expected, which is perpendicular to the minimum principle stress (left-right direction has no stress).

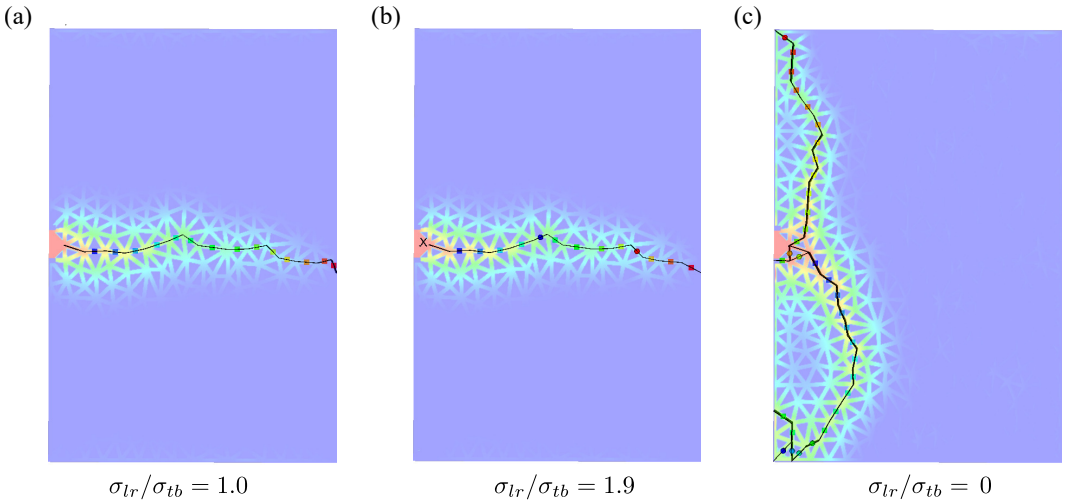

Figure 11. Fracture geometries of cases with different in-situ stress states at 0.04s

Fig. 12 shows the tensile and shear strain of each generated fracture in Fig. 11. The fractures are dominated by tensile fractures, but the shear fractures tend to increase with the anisotropy level. In addition, compared with the cases with no stress imposed (Fig. 4a), several tensile fractures have significant shear strain components.

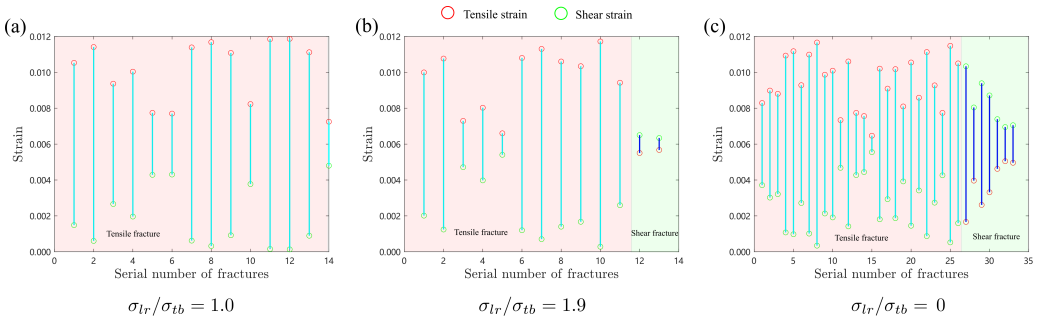

Figure 12. Tensile and shear strain of each fracture segment in Fig. 11

3.4 Impact of heterogeneous bond strengths

To investigate the heterogeneous characteristic of natural rocks, we choose different values of m in the Weibull distribution to make the bond strength vary. The average bond strength is 0.01 and six values of m are chosen for the consideration: $m = 2, 3, 5, 10, 20, 30$, A smaller m value represents a higher heterogeneity degree. For the case with $m = 2$, the strength distribution and the fitting curve are shown in Fig. 13. The fitting parameters are 0.0097 for the mean and 2.04 for the shape factor, m. Therefore, the chosen quantity of particles (741) is sufficient to recover the prescribed distribution for the heterogeneous bond strengths.

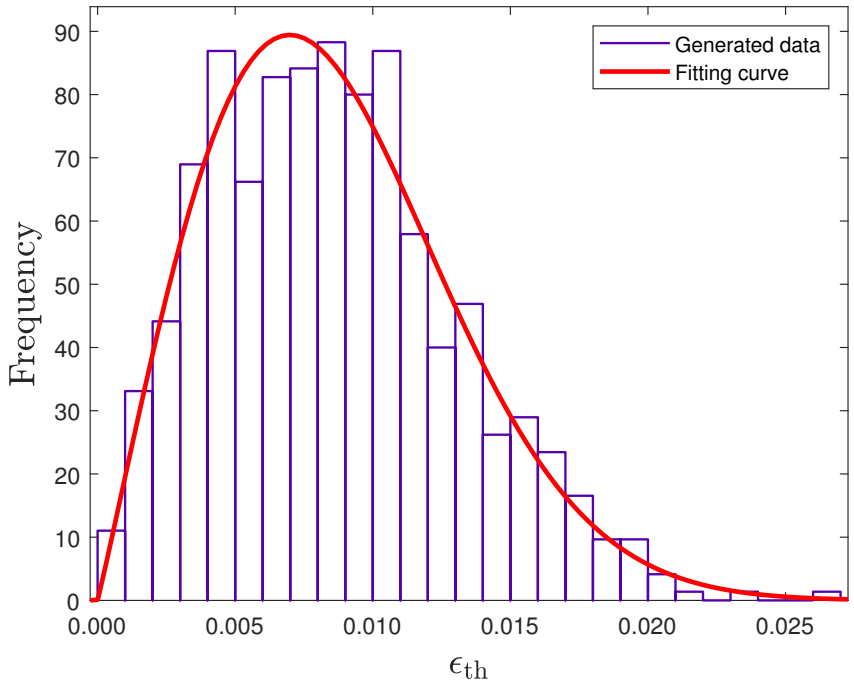

Figure 13. A Weibull distribution fitting of heterogeneous bond strengths

The pore pressure variations of each case at the record point are shown in Fig. 14. The pressure buildup process is the same for all cases with different heterogeneity. However, the initiation pressure is higher for cases with more homogeneous levels. The most heterogeneous case, where $m = 2.0$, has the lowest initiation pressure.

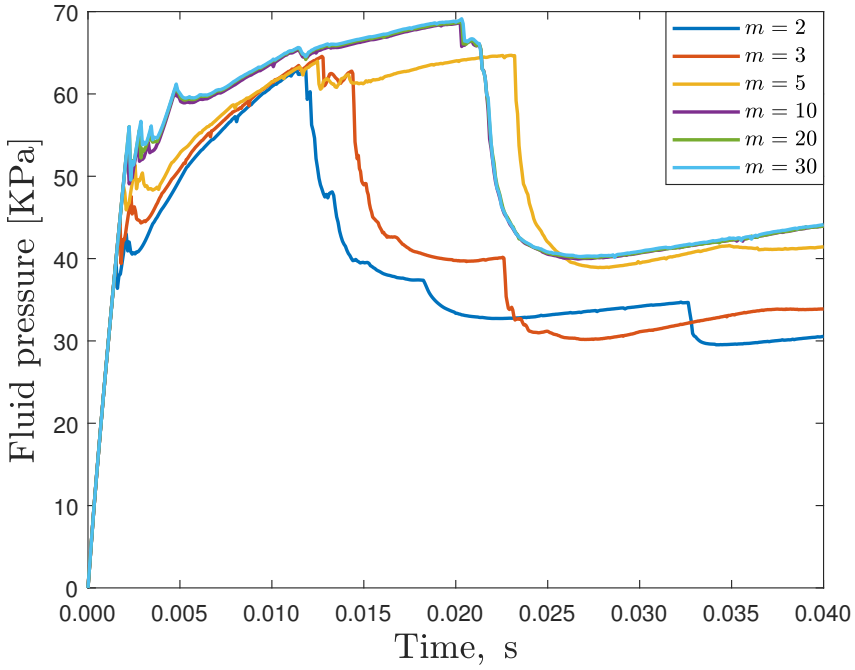

404 **Figure 14.** The pore pressure evolution at the record point for cases with different heterogeneity
405 degrees of bond strengths

412 The fracture geometries of each case are shown in Fig. 15. The higher the heterogeneity
413 degree is, the more complex the fracture geometry is. For the case with $m = 2.0$, the frac-
414 ture geometries are the most complex with several branches. There are also some fractures
415 disconnected from the main fractures, which are caused by the leakage of fluid into the
416 matrix. To better demonstrate this process, the fracture traces are plotted with the bond
417 strength and generation sequence marked in Fig. 16. Most disconnected fractures are shear
418 fractures and their bond strengths are quite low as shown in Fig. 16(b). For the disconnected
419 fractures, the leakage of injected fluid can enhance the pore pressure therein and the high
420 pressure in the main hydraulic fracture can increase the local principal stresses. The in-
421 creased principal stresses usually stifle possible microseismicity from occurring as concluded
422 in N. R. Warpinski et al. (2001) and Zhu et al. (2022). However, there are no initial stresses
423 applied in this simulation, therefore, the increase of principle stresses and pore pressure can
424 trigger the shear failure or even tensile failure of those weak bonds.

428 For more homogeneous cases, where m is large, the fracture geometries do not change
429 significantly. However, compared with a completely homogeneous case (Fig. 3a), there are
430 two main fracture traces instead of a single horizontal one. This fracture geometry is similar

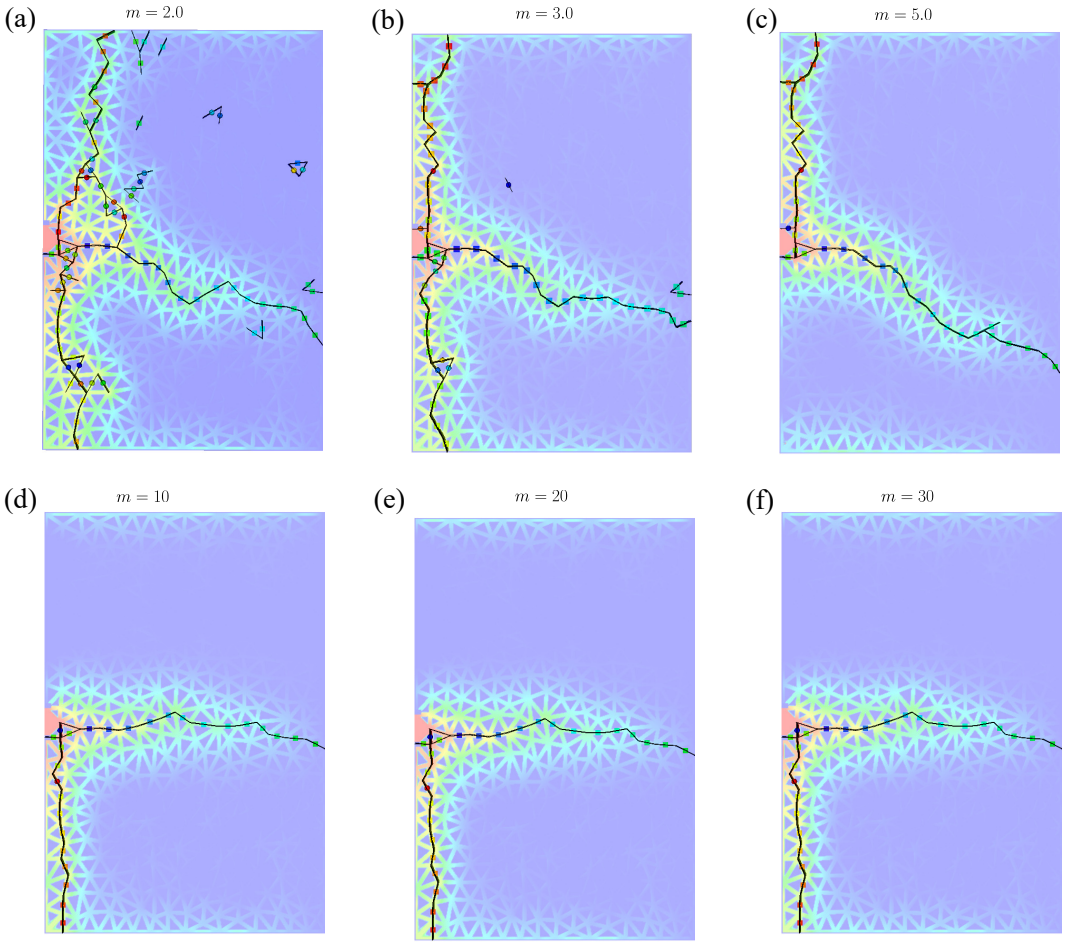

410 **Figure 15.** Fracture geometries of cases with different heterogeneity degrees of bond strengths
411 at 0.04s

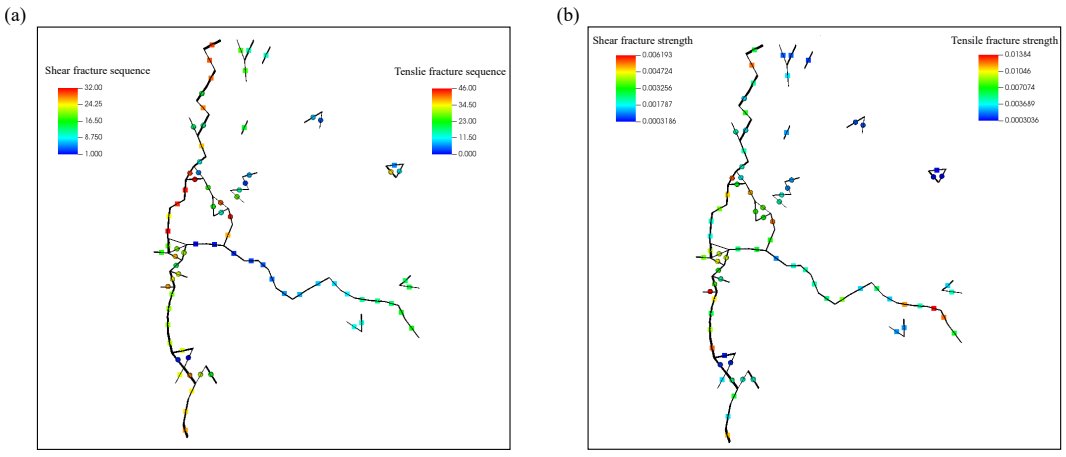

425 **Figure 16.** The generation sequence (a) and bond strength (b) of each fracture segment

to the experiment results in Liu et al. (2018) as shown in Fig. 17 since the actual rocks are not completely homogeneous. Similar patterns do support the correctness of the numerical method in this work.

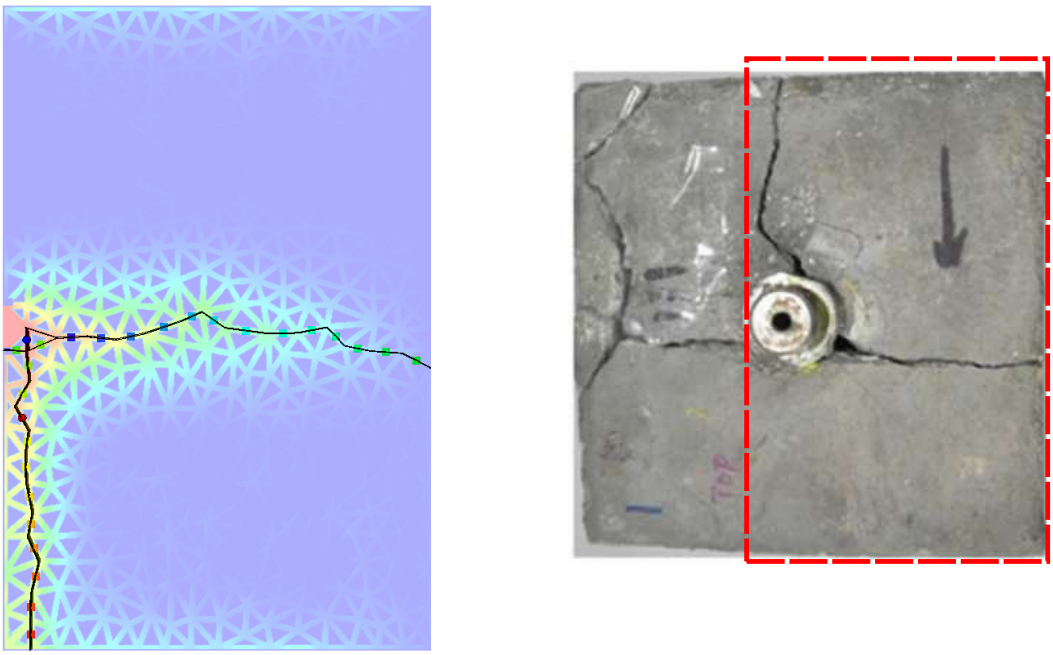

Figure 17. A comparison of fracture geometries with results in a lab experiment (Liu et al., 2016)

The strain components of each fracture in Fig. 15 are shown in Fig. 18. For highly heterogeneous cases, many shear fractures are generated. For the most heterogeneous case, 32 out of 78 fractures are shear fractures, corresponding to a proportion of 41%. With the heterogeneity degree decreases, the proportion of shear fractures decreases sharply and tensile fractures are dominated.

3.5 Impact of formation permeability

The solid volume fraction (γ) has a negative correlation with the formation permeability. A larger γ indicates that more voids are occupied by impermeable solids and the corresponding formation permeability is lower. Impacts of different values of solid volume fractions (γ) are evaluated and six values are chosen: $\gamma = 0.85, 0.9, 0.92, 0.95, 0.97, 0.99$.

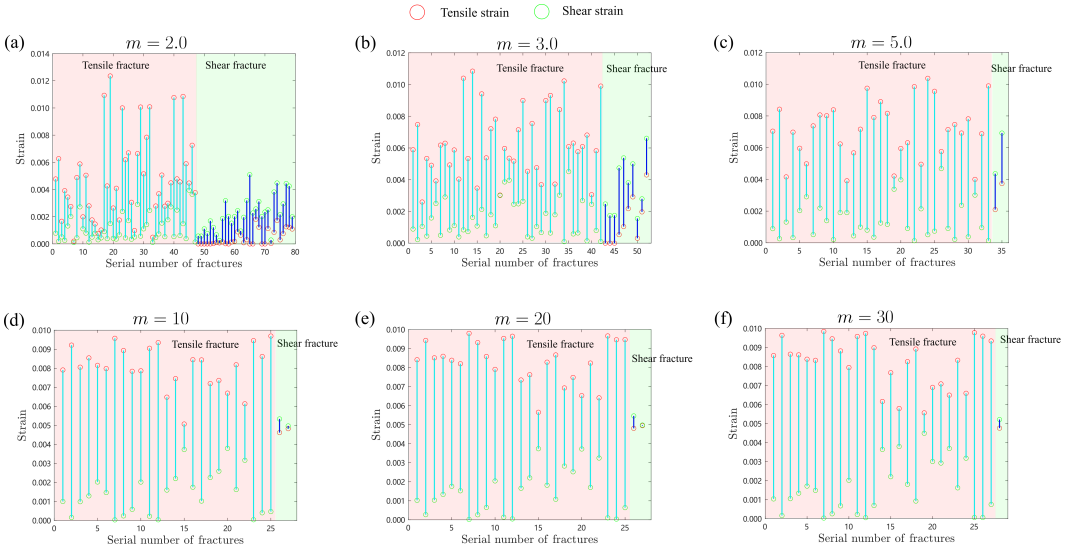

Figure 18. Tensile and shear strain of each fracture segment in Fig. 15

The pore pressure variations at the record point for different cases are shown in Fig. 19. The pressure evolution curves have similar shapes. The lower the matrix permeability, the

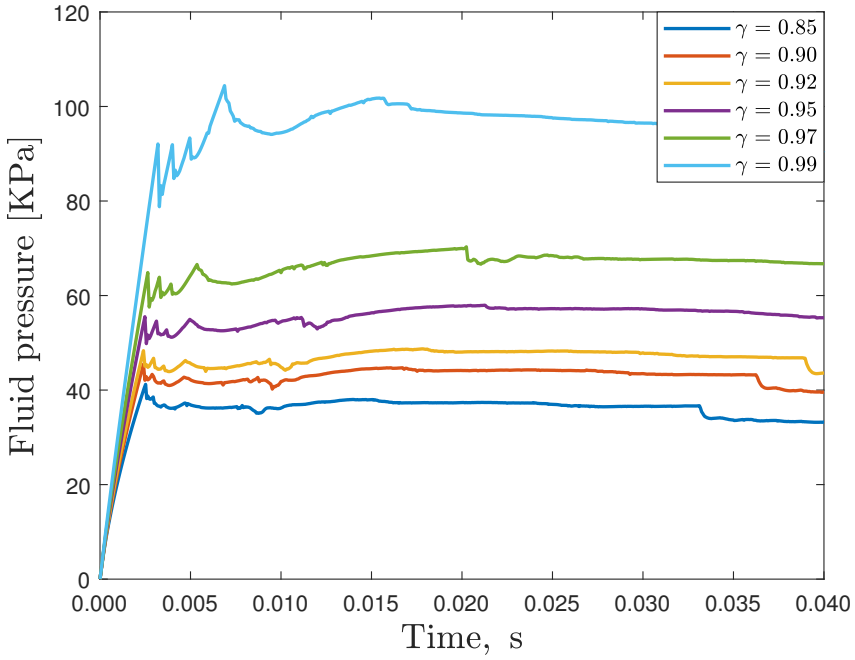

Figure 19. The pore pressure evolution at the record point for cases with different matrix permeability

higher the fracture initiation pressure is, which is consistent with the observations in the

lab experiments (Fazio et al., 2021). The fracture geometries are similar for all cases, which are horizontal. Three examples with $\gamma = 0.85, 0.92$ and 0.99 are shown in Fig. 20. The corresponding strain components of each fracture are shown in Fig. 21. All generated fractures are tensile fractures with insignificant shear strain.

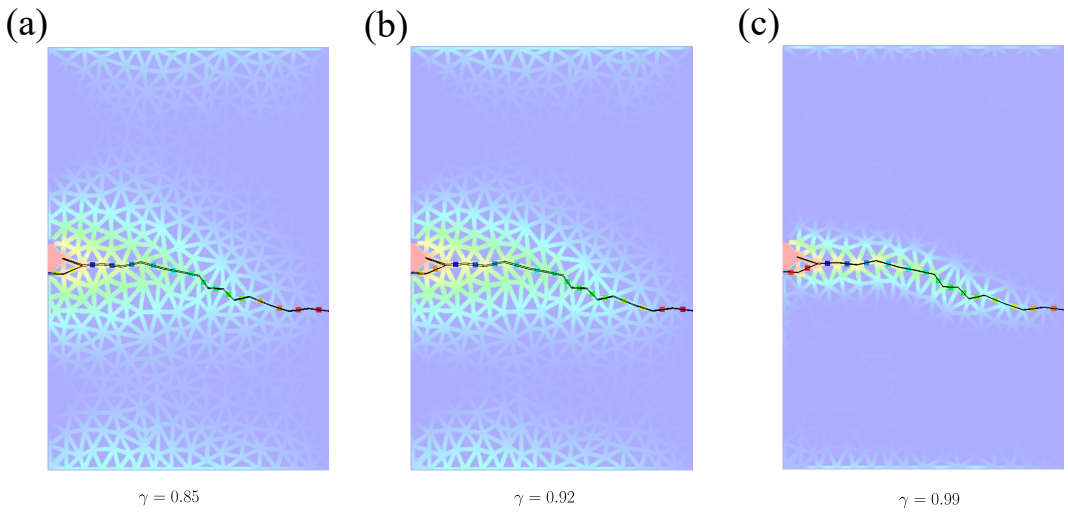

Figure 20. Fracture geometries of cases with different formation permeability at 0.04s

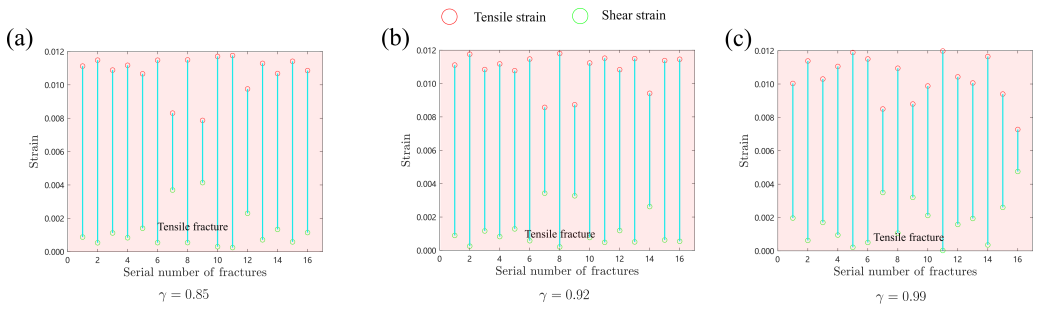

Figure 21. Tensile and shear strain of each fracture segment in Fig. 20

The matrix permeability controls the leakage of fluid as shown in Fig. 20. The pressure propagates to a larger region in a highly permeable case (Fig. 20a) and the influential region is quite narrow for the weakly permeability cases (Fig. 20c). To better demonstrate this phenomenon, the pressure distributions at the fracture initiation of the case with $\gamma = 0.85$ and $\gamma = 0.99$ are shown in Fig. 22. For the case with $\gamma = 0.99$, the pore pressure is quite high in the cave and the preset fracture but hardly propagates to the neighboring region. For the case with $\gamma = 0.85$, the pressure propagates to a much larger region.

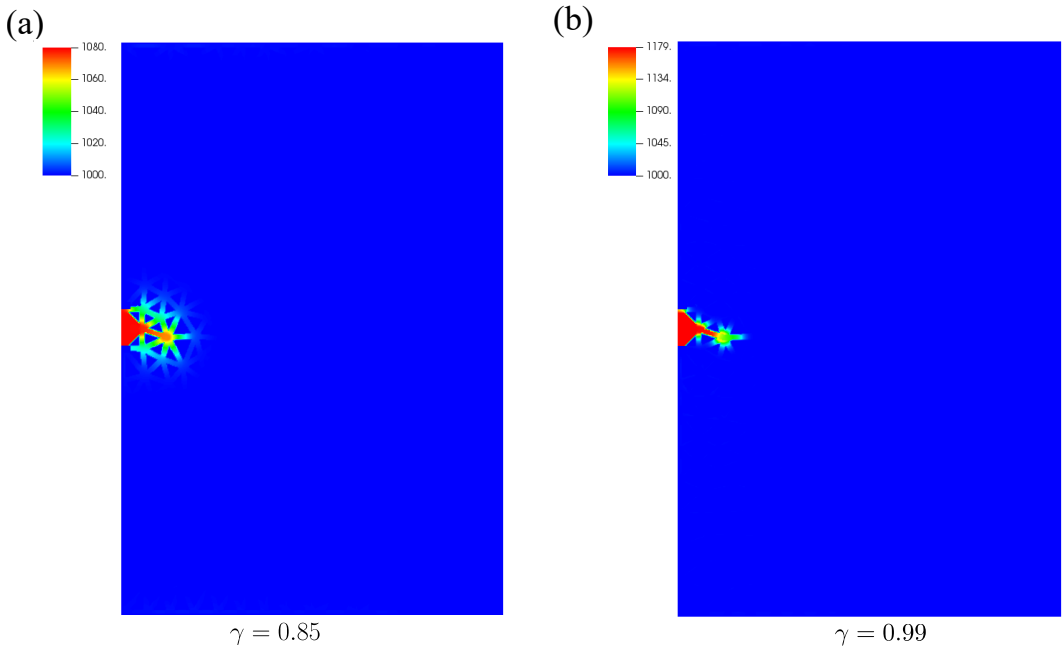

Figure 22. Pore pressure distribution at the fracture initiation stage for cases with a high (a) and low (b) formation permeability, respectability

4 Discussions

In this work, we conducted a systematical analysis of the impacts of different factors (formation parameters, treatment parameters, and rock properties) on the fracture initiation and propagation process. The impact of each factor is evaluated with the other factors fixed. It is beneficial to first have an independent factor analysis and provide a comprehensive and detailed understanding of each factor. Subsequently, analysis of coupled effects or impacts of interactions between different factors can be extended, which is technically available with the foundation constructed in this work. In addition, with optimization of the algorithm efficiency and development of new modulus, more factors, such as temperature, grain size, different injection schemes, can be considered in the future for more complex scenarios.

Most primary hydraulic fractures (horizontal ones in most cases) are tensile fractures. However, when the primary fracture reaches the right boundary, vertical tensile fractures are possible if the pore pressure is high enough. In the transition zone, shear fractures are more dominant than tensile fractures, like Fig. 3(d-f), Fig. 7(b), and Fig. 15(a-c). The generated shear fractures are usually inclined and a Mohr's circle analysis may explain this phenomenon. In Fig. 23, a Morh's circle and stress states of three planes (blue, green, and

red) are determined by the intersection point between the plane and the Mohr's circle. For the demonstration purpose, the friction coefficient is 0.4 and the cohesion strength is set to zero. The specific Mohr's circle in the simulation domain is caused by the enhanced pore pressure from leak-off and principle stresses generated by the compression from the primary hydraulic fracture. The purple arc in Morh's circle refers to all possible plane directions that can trigger a shear failure. The inclined bonds are more likely to form shear failures because their orientations fall into the shear failure range.

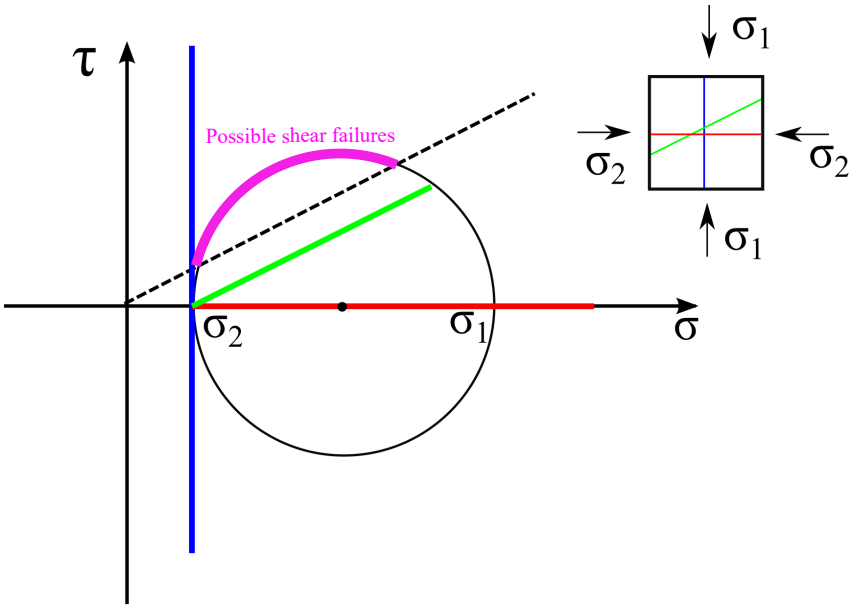

Figure 23. A sketch map of a Mohr's circle for different fracture planes (red, blue, and green)

The DEM-LBM coupled method is powerful to investigate the detailed fracture initiation and propagation process. However, there are still several limitations and two important ones are listed below:

- The roughness of the fracture surface is difficult to be reproduced with DEM since there are large differences in scales between the particle size and asperity size. Therefore the shear dilation process is hard to mimic, which is also an important mechanism to form complex fracture networks in a hydraulic fracturing process (Rahman et al., 2002).
- The breakage of particles is not applicable in this DEM scheme. Therefore, only breakage between particles is possible. However, several experiments observed that

hydraulic fractures can cut the minerals and propagate across particles, especially in hydraulic fracturing with critical CO_2 (Y. Chen et al., 2015),

Therefore, improvements in the numerical scheme or the development of new schemes are still necessary to simulate the hydraulic fracturing process in reality.

5 Conclusions

In this work, a comprehensive investigation of the influential factors on the initiation and propagation in a hydraulic fracturing process is conducted with the DEM-LBM method. The factors include formation parameters (in-situ stress states), treatment parameters (injection rates and fluid viscosity), and rock properties (heterogeneity of rock strengths and formation permeability). Several important findings and conclusions are drawn below:

- All factors have a significant impact on the fracture initiation pressure. A higher injection rate, higher viscosity, and larger in-situ stress will increase the initiation pressure, while a higher formation permeability and higher heterogeneity degree of bond strengths will decrease the initiation pressure.
- Injection rate and heterogeneity degree have much significant impact on the complexity of generated fractures. Fluid viscosity, in-situ stress states, and formation permeability do not change the geometrical complexity.
- Hydraulic fractures are usually tensile fractures, however, they usually do not have pure tensile displacement. Shear fractures are possible and the shear displacement can be significant under certain conditions, such as a high injection rate, and high heterogeneity degrees.

Acknowledgments

This project was supported by the National Key Research and Development Program of China (No. 2019YFA0708704). The authors would like to thank all editors and anonymous reviewers for their comments and suggestions.

Data Availability Statement

The numerical simulation in this work is based on the open-source multi-physics simulation library MechSys developed by Dr. S.A. Galindo Torres. The library is available at `https://mechsys.nongnu.org/`.

Appendix A Benchmark case for LBM simulation

The Poiseuille flow in a slit driven by gravity is chosen as the benchmark case to validate the LBM algorithm. The slit has lengths and widths of 100 and 48 lattice units (lu). A bounce-back boundary condition is implemented on the top and bottom walls. A periodic boundary condition is adopted to avoid the entry or exit effect for the left and right boundaries.

The Reynolds number is 20 to ensure a laminar flow state. The maximum velocity (u_{max}) is chosen as 0.1 $lu\ ts^{-1}$. The relaxation time (τ) is 1.0 for the simple bounce-back boundaries, which yield a kinematic viscosity (ν) of 1/6 $lu^2\ ts^{-1}$. Fluid density (ρ) is chosen as 1.0. The analytical solution for the gravity-driven Poiseuille flow yields a parabolic velocity profile:

$$u(x) = \frac{\rho g}{2\mu}(a^2 - x^2), \tag{A1}$$

where $u(x)$ is the velocity in the Y direction, a is the half width of the slit, g is the gravitational acceleration. The maximum velocity is :

$$u_{max} = \frac{\rho g a^2}{2\mu} \tag{A2}$$

Through rearranging Eq. A2, the corresponding gravitational acceleration (g) to drive the flow is calculated:

$$g = \frac{2\nu u_{max}}{a^2} \tag{A3}$$

Therefore, g is $5.7804 \times 10^{-5}\ lu\ ts^{-2}$.

The velocity distribution in the slit is shown in Fig. A1(a) and Fig. A1(b) shows the comparison between the analytical solution and the simulation result.

Appendix B Benchmark case for the DEM simulation

A Brazilian test is used to validate the correctness of the DEM simulation. A round disc with a diameter of 0.2 m and a thickness of 0.1 m is generated for the simulation. The

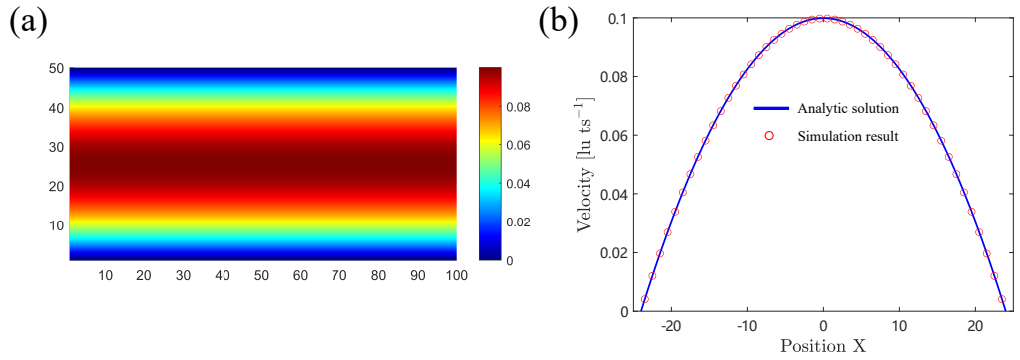

Figure A1. (a) The velocity distribution in a slit (b) Comparison between the analytical solution and LBM result

total number of particles is 1,924. The specific rock properties are not used in the simulation considering the computational cost. The normal and tangential contact stiffness are 1.0×10^5N/m. The normal and tangential elastic modulus are 1.0×10^5Pa. The threshold value on the total strain is 0.02. The time step is chosen as 4.5×10^{-5} s. The breaking results after the compression are shown in Fig. B1. A vertical fracture and V-shaped damage zones are observed, and similar results are found in lab experiments (Gong et al., 2019).

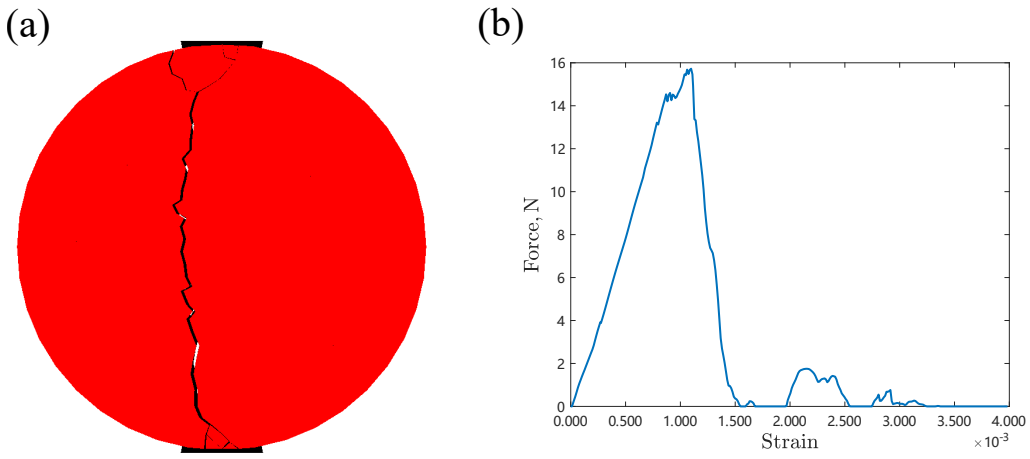

Figure B1. (a) Fractures formed after compression in a Brazilian test (b) The force-strain relation of the Brazilian test

References

Buckingham, E. (1915). The principle of similitude. *Nature*, *96*(2406), 396–397.

Chen, H., Meng, X., Niu, F., Tang, Y., Yin, C., & Wu, F. (2018). Microseismic monitoring of stimulating shale gas reservoir in sw china: 2. spatial clustering controlled by the preexisting faults and fractures. *Journal of Geophysical Research: Solid Earth*, *123*(2), 1659–1672.

Chen, S., & Doolen, G. D. (1998). Lattice boltzmann method for fluid flows. *Annual review of fluid mechanics*, *30*(1), 329–364.

Chen, Y., Nagaya, Y., & Ishida, T. (2015). Observations of fractures induced by hydraulic fracturing in anisotropic granite. *Rock Mechanics and Rock Engineering*, *48*(4), 1455–1461.

Chen, Z., Elsworth, D., & Wang, M. (2020). Does low-viscosity fracturing fluid always create complex fractures? *Journal of Geophysical Research: Solid Earth*, *125*(9), e2020JB020332.

Chen, Z., Jin, X., & Wang, M. (2018). A new thermo-mechanical coupled dem model with non-spherical grains for thermally induced damage of rocks. *Journal of the Mechanics and Physics of Solids*, *116*, 54–69.

Chen, Z., & Wang, M. (2017). Pore-scale modeling of hydromechanical coupled mechanics in hydrofracturing process. *Journal of Geophysical Research: Solid Earth*, *122*(5), 3410–3429.

Chen, Z., & Wang, M. (2020). An improved immersed moving boundary for hydrodynamic force calculation in lattice boltzmann method. *International Journal for Numerical Methods in Engineering*, *121*(20), 4493–4508.

Cheng, S., Zhang, M., Zhang, X., Wu, B., Chen, Z., Lei, Z., & Tan, P. (2022). Numerical study of hydraulic fracturing near a wellbore using dual boundary element method. *International Journal of Solids and Structures*, *239*, 111479.

Cundall, P. A., & Strack, O. D. (1979). A discrete numerical model for granular assemblies. *geotechnique*, *29*(1), 47–65.

Dahi-Taleghani, A., & Olson, J. E. (2011). Numerical modeling of multistranded-hydraulic-fracture propagation: accounting for the interaction between induced and natural fractures. *SPE journal*, *16*(03), 575–581.

De Pater, C., & Beugelsdijk, L. (2005). Experiments and numerical simulation of hydraulic fracturing in naturally fractured rock. In *Alaska rocks 2005, the 40th us symposium*

on rock mechanics (usrms).

Duan, K., Kwok, C. Y., Wu, W., & Jing, L. (2018). Dem modeling of hydraulic fracturing in permeable rock: influence of viscosity, injection rate and in situ states. *Acta Geotechnica*, *13*(5), 1187–1202.

Fazio, M., Ibemesi, P., Benson, P., Bedoya-González, D., & Sauter, M. (2021). The role of rock matrix permeability in controlling hydraulic fracturing in sandstones. *Rock Mechanics and Rock Engineering*, *54*(10), 5269–5294.

Galindo-Torres, S. (2013). A coupled discrete element lattice boltzmann method for the simulation of fluid–solid interaction with particles of general shapes. *Computer Methods in Applied Mechanics and Engineering*, *265*, 107–119.

Galindo-Torres, S. A., Alonso-Marroquín, F., Wang, Y., Pedroso, D., & Castano, J. M. (2009). Molecular dynamics simulation of complex particles in three dimensions and the study of friction due to nonconvexity. *Physical Review E*, *79*(6), 060301.

Galindo-Torres, S. A., Pedroso, D., Williams, D., & Li, L. (2012). Breaking processes in three-dimensional bonded granular materials with general shapes. *Computer Physics Communications*, *183*(2), 266–277.

Gandossi, L., & Von Estorff, U. (2013). An overview of hydraulic fracturing and other formation stimulation technologies for shale gas production. *Eur. Commisison Jt. Res. Cent. Tech. Reports*, *26347*.

Gong, F., Zhang, L., & Wang, S. (2019). Loading rate effect of rock material with the direct tensile and three brazilian disc tests. *Advances in Civil Engineering*, *2019*.

Goodfellow, S., Nasseri, M., Maxwell, S., & Young, R. (2015). Hydraulic fracture energy budget: Insights from the laboratory. *Geophysical Research Letters*, *42*(9), 3179–3187.

Heider, Y. (2021). A review on phase-field modeling of hydraulic fracturing. *Engineering Fracture Mechanics*, *253*, 107881.

Huang, B., & Liu, J. (2017). Experimental investigation of the effect of bedding planes on hydraulic fracturing under true triaxial stress. *Rock Mechanics and Rock Engineering*, *50*(10), 2627–2643.

Kumari, W., Ranjith, P., Perera, M., Li, X., Li, L., Chen, B., ... De Silva, V. (2018). Hydraulic fracturing under high temperature and pressure conditions with micro ct applications: geothermal energy from hot dry rocks. *Fuel*, *230*, 138–154.

Lecampion, B. (2009). An extended finite element method for hydraulic fracture problems. *Communications in Numerical Methods in Engineering*, *25*(2), 121–133.

Liu, P., Ju, Y., Gao, F., Ranjith, P. G., & Zhang, Q. (2018). Ct identification and fractal characterization of 3-d propagation and distribution of hydrofracturing cracks in low-permeability heterogeneous rocks. *Journal of Geophysical Research: Solid Earth*, *123*(3), 2156–2173.

Liu, P., Ju, Y., Ranjith, P. G., Zheng, Z., Wang, L., & Wanniarachchi, A. (2016). Visual representation and characterization of three-dimensional hydrofracturing cracks within heterogeneous rock through 3d printing and transparent models. *International Journal of Coal Science & Technology*, *3*(3), 284–294.

Mohammadnejad, T., & Khoei, A. (2013). An extended finite element method for hydraulic fracture propagation in deformable porous media with the cohesive crack model. *Finite Elements in Analysis and Design*, *73*, 77–95.

Morgan, S., Li, B., & Einstein, H. (2017). Effect of injection rate on hydraulic fracturing of opalinus clay shale. In *51st us rock mechanics/geomechanics symposium.*

Nagaso, M., Mikada, H., & Takekawa, J. (2015). The role of fluid viscosity in hydraulic fracturing in naturally fractured rock. In *Seg technical program expanded abstracts 2015* (pp. 3214–3218). Society of Exploration Geophysicists.

Noble, D., & Torczynski, J. (1998). A lattice-boltzmann method for partially saturated computational cells. *International Journal of Modern Physics C*, *9*(08), 1189–1201.

Olson, J. E., & Taleghani, A. D. (2009). Modeling simultaneous growth of multiple hydraulic fractures and their interaction with natural fractures. In *Spe hydraulic fracturing technology conference.*

O'Sullivan, C., & Bray, J. D. (2004). Selecting a suitable time step for discrete element simulations that use the central difference time integration scheme. *Engineering Computations*.

Pan, X.-H., Xiong, Q.-Q., & Wu, Z.-J. (2018). New method for obtaining the homogeneity index m of weibull distribution using peak and crack-damage strains. *International Journal of Geomechanics*, *18*(6), 04018034.

Papachristos, E., Scholtès, L., Donzé, F., & Chareyre, B. (2017). Intensity and volumetric characterizations of hydraulically driven fractures by hydro-mechanical simulations. *International Journal of Rock Mechanics and Mining Sciences*, *93*, 163–178.

Peirce, A., & Detournay, E. (2009). An eulerian moving front algorithm with weak-form tip asymptotics for modeling hydraulically driven fractures. *Communications in numerical methods in engineering*, *25*(2), 185–200.

Pruess, K. (2006). Enhanced geothermal systems (egs) using co2 as working fluid—a novel approach for generating renewable energy with simultaneous sequestration of carbon. *Geothermics*, *35*(4), 351–367.

Rahman, M., Hossain, M., & Rahman, S. (2002). A shear-dilation-based model for evaluation of hydraulically stimulated naturally fractured reservoirs. *International Journal for Numerical and Analytical Methods in Geomechanics*, *26*(5), 469–497.

Shimizu, H., Murata, S., & Ishida, T. (2011). The distinct element analysis for hydraulic fracturing in hard rock considering fluid viscosity and particle size distribution. *International journal of rock mechanics and mining sciences*, *48*(5), 712–727.

Stanchits, S., Surdi, A., Gathogo, P., Edelman, E., & Suarez-Rivera, R. (2014). Onset of hydraulic fracture initiation monitored by acoustic emission and volumetric deformation measurements. *Rock Mechanics and Rock Engineering*, *47*(5), 1521–1532.

Van Mier, J. G., van Vliet, M. R., & Wang, T. K. (2002). Fracture mechanisms in particle composites: statistical aspects in lattice type analysis. *Mechanics of Materials*, *34*(11), 705–724.

Wang, Y., Li, X., & Tang, C. (2016). Effect of injection rate on hydraulic fracturing in naturally fractured shale formations: a numerical study. *Environmental Earth Sciences*, *75*(11), 1–16.

Wangen, M. (2011). Finite element modeling of hydraulic fracturing on a reservoir scale in 2d. *Journal of Petroleum Science and Engineering*, *77*(3-4), 274–285.

Warpinski, N., Wolhart, S., & Wright, C. (2004). Analysis and prediction of microseismicity induced by hydraulic fracturing. *Spe Journal*, *9*(01), 24–33.

Warpinski, N. R., Wolhart, S., Wright, C., et al. (2001). Analysis and prediction of microseismicity induced by hydraulic fracturing. In *Spe annual technical conference and exhibition.*

Wilson, Z. A., & Landis, C. M. (2016). Phase-field modeling of hydraulic fracture. *Journal of the Mechanics and Physics of Solids*, *96*, 264–290.

Yousefi, A., & Ng, T.-T. (2017). Dimensionless input parameters in discrete element modeling and assessment of scaling techniques. *Computers and Geotechnics*, *88*, 164–173.

Yushi, Z., Shicheng, Z., Tong, Z., Xiang, Z., & Tiankui, G. (2016). Experimental investigation into hydraulic fracture network propagation in gas shales using ct scanning technology. *Rock Mechanics and Rock Engineering*, *49*(1), 33–45.

Zeng, Z., & Roegiers, J.-C. (2002). Experimental observation of injection rate influence on

the hydraulic fracturing behavior of a tight gas sandstone. In *Spe/isrm rock mechanics conference.*

Zhao, X., Huang, B., & Xu, J. (2019). Experimental investigation on the characteristics of fractures initiation and propagation for gas fracturing by using air as fracturing fluid under true triaxial stresses. *Fuel*, *236*, 1496–1504.

Zhao, Y., Zhang, Y., Wang, C., & Liu, Q. (2022). Hydraulic fracturing characteristics and evaluation of fracturing effectiveness under different anisotropic angles and injection rates: an experimental investigation in absence of confining pressure. *Journal of Natural Gas Science and Engineering*, *97*, 104343.

Zhu, W., He, X., Khirevich, S., & Patzek, T. W. (2022). Fracture sealing and its impact on the percolation of subsurface fracture networks. *J. Pet. Sci. Eng.*, *218*, 111023.

Zhuang, L., Kim, K. Y., Jung, S. G., Diaz, M., & Min, K.-B. (2019). Effect of water infiltration, injection rate and anisotropy on hydraulic fracturing behavior of granite. *Rock Mechanics and Rock Engineering*, *52*(2), 575–589.

Zhuang, L., & Zang, A. (2021). Laboratory hydraulic fracturing experiments on crystalline rock for geothermal purposes. *Earth-Science Reviews*, *216*, 103580.